

Physical limits on galvanotaxis

Ifunanya Nwogbaga,^{1,*} A Hyun Kim,^{1,*} and Brian A. Camley^{1,2}

¹*Department of Biophysics, Johns Hopkins University*

²*Department of Physics & Astronomy, Johns Hopkins University*

Eukaryotic cells of many types can polarize and migrate in response to electric fields via “galvanotaxis”; this ability helps skin cells heal wounds. Recent experimental evidence suggests galvanotaxis occurs because membrane proteins redistribute via electrophoresis, though the sensing species has not yet been conclusively identified. We use a physical model to show that stochasticity due to the finite number of sensing proteins limits the accuracy of galvanotaxis via electrophoresis. Using maximum likelihood estimation, we show how cells can best interpret this noisy signal, and how their accuracy should depend on the cell size and electric field strength. Our model can be fit well to data measuring galvanotaxis of keratocytes, neural crest cells, and granulocytes. Our results show that eukaryotic cells can likely achieve experimentally observed directionalities with either a relatively small number (around 100) of highly-polarized proteins, or a large number ($\sim 10^4$) of proteins with a relatively small change in concentration across the cell ($\sim 7\%$ change from cathode to anode). This may explain why identifying the sensor species has been difficult, as candidates need not be strongly polarized even in large electric fields. A second prediction of the model is that the accuracy of cells in predicting the electric field direction only weakly depends on their size.

Eukaryotic cells will migrate in response to an applied electrical field – a process called “galvanotaxis” or “electrotaxis” [1]. The response to electric fields helps give a directional response to wound healing [2] and immune response [3], and can override other guidance cues like chemical signals [4]. While galvanotactic responses have been systematically measured for decades, understanding of the mechanisms of galvanotaxis pale in comparison to the understanding of chemotaxis [1]. The current best-supported theory is that galvanotaxis arises because of migration of a sensor species on the surface of the cell in response to the electric field [5–7] (ciliated cells may also have an alternate type of galvanotaxis [8]). There has been a revival of interest in galvanotaxis, in part driven by experiments showing how effective a tool it can be to control groups of cells [9–14]. Recent models [15, 16] and older works [17, 18] have also described galvanotaxis of single cells phenomenologically in terms of a repolarization of cell orientation to follow the field.

Within the study of chemotaxis, there is strong evidence that both eukaryotic cells and bacteria can sense at nearly the limits imposed on them by basic physical and statistical principles [19–25]. This is part of the broader interest in finding fundamental physical bounds for accuracy [26–31]. Here, we ask the complementary question for galvanotaxis: how precisely can a cell sense the direction of an applied electrical field? Our strategy will be to write a model for the probability of observing a sensor configuration in the field, and then determine how the cell can best estimate the field angle by choosing an estimated direction $\hat{\psi}$ that maximizes the likelihood of observing this configuration, building off past maximum-likelihood results [31–36]. We will also derive results bounding the best possible estimation cells can

make of the field position given the unavoidable randomness in sensor positions.

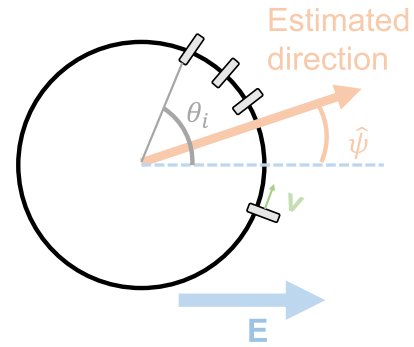


FIG. 1. Illustration of sensors on surface of cell. The cell uses the stochastic locations of these sensors ($\theta_1, \theta_2, \dots, \theta_N$) to make a noisy estimate $\hat{\psi}$ of the field’s true direction.

We apply a simple model, assuming that a receptor – or other charged molecule – migrates on the surface of the cell in response to an electric field. We call this a *sensor*. Our assumption is that the velocity of the sensor species is proportional to the component of the electric field in the membrane’s tangent plane [37], i.e. $\mathbf{v} = \mu [\mathbf{E} - (\mathbf{E} \cdot \hat{\mathbf{n}})\hat{\mathbf{n}}]$ where $\hat{\mathbf{n}}$ is a local normal to the surface of the cell. The parameter μ , which can be positive or negative, includes the effect of electrophoresis and electroosmotic flow, and can be estimated from microscopic properties of the sensor and environment [6, 7, 37]; in this paper, we will view it as purely a phenomenological value. Assuming this model, the probability flux due to flow and diffusion on the surface is $\mathbf{J} = \mathbf{v}p - D\nabla_S p$ where p is the probability density on the surface, D is the sensor diffusion coefficient, and ∇_S the gradient on the surface. The continuity equation is then $\frac{\partial p}{\partial t} = -\nabla_S \cdot \mathbf{J}$. Let’s first consider a two-dimensional model of a cell as a circle (Fig. 1). In this case, positions on the cell surface are param-

* These two authors contributed equally

eterized by a single angle θ , and $\nabla_S \rightarrow \frac{1}{R} \partial_\theta$. For our circle, the velocity is $\mathbf{v} = \mu [\mathbf{E} - (\mathbf{E} \cdot \hat{\mathbf{n}})\hat{\mathbf{n}}] = \mu(\mathbf{E} \cdot \hat{\boldsymbol{\theta}})\hat{\boldsymbol{\theta}}$, where $\hat{\boldsymbol{\theta}} = (-\sin \theta, \cos \theta)$ is the local tangent. Our continuity equation becomes, if the electrical field is in the $\hat{\mathbf{x}}$ direction,

$$\frac{\partial}{\partial t} p(\theta, t) = \frac{1}{R} \frac{\partial}{\partial \theta} [\mu E \sin \theta p(\theta, t)] + \frac{D}{R^2} \frac{\partial^2}{\partial \theta^2} p(\theta, t). \quad (1)$$

The steady-state solution to this equation is $p(\theta) = Z^{-1} e^{\kappa \cos \theta}$, where $\kappa = \mu ER/D$ and Z is a normalizing factor that does not depend on θ . This probability density is a von Mises distribution – one way of generalizing the Gaussian distribution to a periodic domain [38]. The concentration κ reflects how precisely sensors are localized around the field: when $\kappa \gg 1$, the von Mises distribution will become a Gaussian with variance $1/\kappa$. We will often think about how cell responses depend on electric field, so we also define $\beta = \mu R/D$ so $\kappa = \beta E$.

When the electric field has orientation ψ relative to the x axis, we can simply rotate our coordinate system to find $p(\theta) = Z^{-1} e^{\kappa \cos(\theta - \psi)}$. The cell can choose an optimal orientation ψ by maximizing the likelihood of ψ given its observation of the N sensor locations $\boldsymbol{\theta} = (\theta_1, \theta_2, \theta_3, \dots, \theta_N)$, where this likelihood is $\mathcal{L}(\psi, E; \boldsymbol{\theta}) = p(\boldsymbol{\theta} | \psi, E)$. If the sensor positions are independent, then $\mathcal{L}(\psi, E; \boldsymbol{\theta}) = \prod_{i=1}^N p(\theta_i | \psi, E)$, or

$$\begin{aligned} \ln \mathcal{L}(\psi, E; \boldsymbol{\theta}) &= -N \ln Z + \kappa \sum_{i=1}^N \cos(\theta_i - \psi) \quad (2) \\ &= -N \ln Z + \beta \mathbf{E} \cdot \boldsymbol{\rho}, \quad (3) \end{aligned}$$

where $\boldsymbol{\rho} = \sum_i (\cos \theta_i, \sin \theta_i)$ is the sum of sensor positions. Given $\boldsymbol{\theta}$, the direction ψ that maximizes $\ln \mathcal{L}$ is the maximum likelihood estimator of the field direction ψ ; we call this estimator $\hat{\psi}$. We can see directly from Eq. 3 that the log-likelihood is maximized if the field is in the direction of the sum of sensor locations $\boldsymbol{\rho}$, i.e. $\tan \hat{\psi} = \sum_i \sin \theta_i / \sum_i \cos \theta_i$ if $\beta > 0$; see also Appendix D.

The precision with which a cell can sense the direction ψ is limited by the Fisher information $I(\psi) = -\langle \frac{\partial^2 \ln \mathcal{L}}{\partial \psi^2} \rangle$ [39], which can be computed as $I(\psi) = \kappa \sum_{i=1}^N \langle \cos(\theta_i - \psi) \rangle$. Using the properties of the von Mises distribution, this is

$$I(\psi) = N \kappa I_1(\kappa) / I_0(\kappa) \quad (\text{circle}), \quad (4)$$

where $I_m(x)$ is a modified Bessel function of the first kind. This is also a known result in terms of independent von Mises measurements [38]. We can also compute Fisher information and maximum likelihood estimators for sensors on a sphere, extending [37] (see Appendix C, D).

$$I(\psi) = N(\kappa \coth \kappa - 1) \quad (\text{sphere}). \quad (5)$$

Unbiased estimators $\hat{\psi}$ of a parameter ψ are limited by the Cramer-Rao bound,

$$\langle (\hat{\psi} - \psi)^2 \rangle \geq 1/I(\psi) \quad (\text{Cramer-Rao}). \quad (6)$$

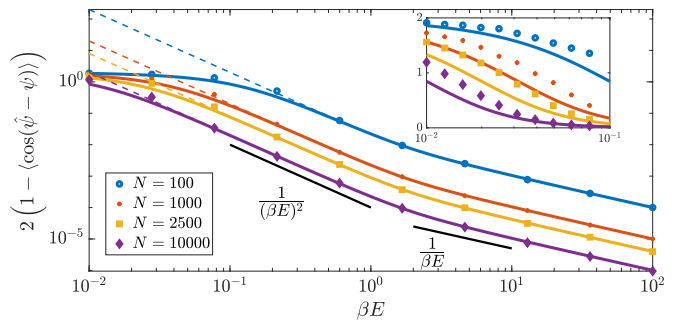


FIG. 2. Accuracy of galvanotactic estimation as a function of electric field and number of sensors. Solid lines are the simple periodic bound (Eq. 7), dashed lines are the normal Cramer-Rao bound (Eq. 6), symbols are stochastic simulation. $d = 2$ (circle) shown here; Appendix C has an analogous figure for the sphere. Inset shows zoomed in region in linear scale, showing MLE variance is systematically above Eq. 7.

However, this bound can be incorrect when estimating a direction like ψ when $I(\psi)$ is small. The condition for an estimator to be unbiased, $\langle \hat{\psi} \rangle = \psi$, will not be fulfilled for estimators that could vary modulo 2π . It is possible to extend the Cramer-Rao bound to variables defined on a circle [38]. A simplified version of these results are

$$\langle \cos(\hat{\psi} - \psi) \rangle \leq \sqrt{\frac{I(\psi)}{1 + I(\psi)}} \quad (\text{periodic Cramer-Rao}). \quad (7)$$

A brief derivation is shown in Appendix A.

We show how the predicted accuracy of a galvanotaxing cell depends on the field strength E , the number of sensors N , and β in Fig. 2 for a circular cell. We plot the circular equivalent of the variance, which we call $V \equiv 2(1 - \langle \cos(\hat{\psi} - \psi) \rangle)$; when the variance is small, this reduces to the ordinary variance, as can be seen from a Taylor expansion. We compute this variance via the periodic Cramer-Rao bound, Eq. 7 (solid lines), and via stochastic simulation (symbols). In the stochastic simulation, we generate sensor positions according to the von Mises distribution $p(\theta) \sim e^{\kappa \cos(\theta - \psi)}$, then for each sensor configuration, we determine the direction $\hat{\psi}$ that maximizes the log-likelihood by computing the sum of sensor positions $\boldsymbol{\rho}$. We then compute the average $2(1 - \langle \cos(\hat{\psi} - \psi) \rangle)$ over 5000 generated sensor configurations. We also show the ordinary Cramer-Rao bound $1/I(\psi)$.

In Fig. 2, the error in orientation generally scales as $1/(\beta E)^2$ when βE is in intermediate ranges (0.1-1) and scales as $1/\beta E$ at large fields. This reflects the properties of the Fisher information – at small κ , $I(\psi) \approx N\kappa^2/d$ with $d = 2, 3$ for circle and sphere, respectively. At large κ , $I(\psi) \sim N\kappa$ for both circle and sphere. For much of the range of parameters shown in Fig. 2, the circular variance V agrees well with the ordinary Cramer-Rao bound (dashed line, Eq. 6), with $V \approx 1/I(\psi)$. However, when there is less information about the field direction,

$1/I(\psi)$ exceeds the maximum possible $V = 2$, and the periodic Cramer-Rao bound is a better measure of the simulated variance. However, the bound in Eq. 7 is not “tight” – the maximum likelihood estimator does not achieve the best possible variance at small βE (inset to Fig. 2).

Comparison with experiment. Our theory for accuracy depends on a known electric field, as well as the coefficient β and the number of sensors N . Without an established identity of the sensor, estimating N is difficult. Receptors like EGFR which may play a role in galvanotaxis [40] can have expression levels of $\sim 50,000$ receptors/cell [41], but other putative sensors [42] would likely be fewer in number. We can estimate β for a given molecule given its polarized distribution in an electric field. Recent work has measured the distribution of fluorescent tdTomato-GPI in electric fields, observing the ratio of cathode/anode fluorescence is roughly 2.0 at a field strength of 1000 V/m [7], and showing that this is consistent with an electromigration model [6, 7, 37]. 1000 V/m is a relatively strong field, as cells can develop directed migration in fields of ~ 10 V/m [17]. In the electromigration model we apply, for both circular and spherical cells, the ratio between the cathodal-side and anodal-side probability density is $e^{2\kappa}$. The data on tdTomato-GPI is consistent with a value of $e^{2\kappa} = 2$, or $\kappa \approx 0.35$ at $E = 1000$ V/m, or $\beta \approx (0.35)/(1000 \text{ V/m}) \approx 3.5 \times 10^{-4}$ m/V. Thus, even at the largest fields, we see $\kappa < 1$, so we expect the weak-field result $I(\psi) \approx N\kappa^2/d$ to be appropriate. If this is the case, the dependence on the electric field given by Eq. 7 will be relatively simple – we expect the cosine of the cell’s orientation to be $\sqrt{N\kappa^2 d^{-1}/(1 + N\kappa^2 d^{-1})} \equiv \sqrt{\gamma^2 E^2/(1 + \gamma^2 E^2)}$, where we have collected all the unknowns into $\gamma^2 \equiv N\beta^2/d$, a single remaining fit parameter. We show in Fig. 3 three experimental measurements of galvanotaxis in different cell types: keratocytes [43], and neural crest and granulocytes [17]. These experiments are typically reported in terms of the cosine of the angle of cell velocity relative to the electric field – we write this as $\langle \cos(\hat{\psi} - \psi) \rangle$, essentially assuming that the cell’s velocity is its best estimate of the field direction. All these measurements can

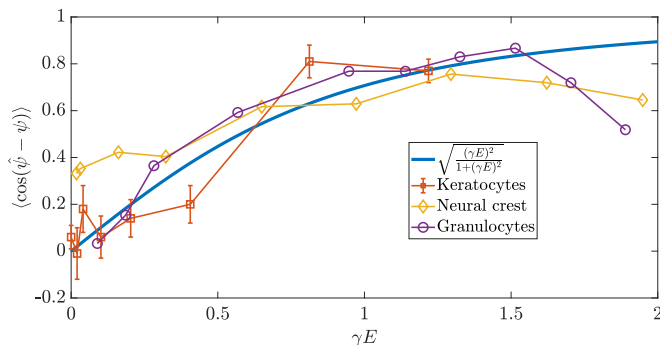


FIG. 3. Fits to experimental data. γ -values are 2×10^{-3} m/V, 3.3×10^{-3} m/V, and 1.9×10^{-3} m/V for keratocytes, neural crests, and granulocytes, respectively.

be reasonably collapsed onto the single curve predicted by our model by fitting only a single cell-type-dependent parameter γ , though there are deviations at small electric field for the neural crest cells and large electric fields for neural crest and granulocytes. Large-field deviations may arise from heating [5]. A similar collapse of neural crest and granulocyte data was discovered by [17], though without identifying this form. Because the only relevant fitting parameter is $\gamma^2 \equiv N\beta^2/d$, we cannot separately determine N and β – i.e. we cannot tell how much of the cell’s accuracy is driven by having a large number of sensors vs sensors that are highly polarized. If we use the estimate $\beta \approx 3.5 \times 10^{-4}$ m/V found from tdTomato-GPI experiments on CHO cells and assume $d = 3$, this would imply that these three cell types all have roughly 90-270 sensors. By contrast, if we assume that the field sensor is expressed at a level similar to typical chemoattractant receptors, guessing $N \approx 10,000$, then we find $\beta \approx (3 - 6) \times 10^{-5}$ m/V for the cell types studied here. This would correspond to a cathode/anode fluorescence ratio of $e^{2\beta E} \approx 1.07 - 1.12$ at $E = 1000$ V/m. This implies that *the sensor may not need to be strongly polarized, even at large fields* – similar to the observation that as few as a hundred bound receptors’ difference between front and back may lead to chemotactic migration [24].

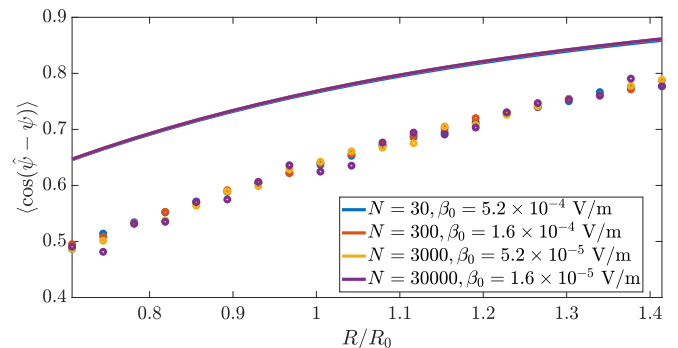


FIG. 4. Dependence on cell radius is relatively weak. Lines are the bound (Eq. 7 with Eq. 4), symbols are stochastic simulation, as in Fig. 2. $\gamma^2 = N\beta^2/d$ is fit to the data of [43], $\gamma = 0.002$ m/V, and the E field used is 600 V/m. $d = 2$.

Accuracy depends weakly on size for typical cell area ranges. Sun et al. observed that the accuracy of keratocyte galvanotaxis is not notably dependent on radius (Fig. S3C of [43]). How consistent is this with the predictions of our model? How much does an increased cell size increase accuracy? The functional dependence of directionality $\langle \cos(\hat{\psi} - \psi) \rangle$ on radius and electric field is identical, as our results depend only on $\kappa = \mu RE/D$, but unlike electric fields, cell areas only vary \sim twofold [43]. For small κ , as appropriate to the experiments, $I(\psi) \sim \kappa^2 \sim R^2$. The periodic Cramer-Rao bound shows the cosine of the angle of the cell’s motion from the field is $\sqrt{I(\psi)/(1 + I(\psi))}$, so we would expect that the cosine of the angle would increase no faster than linear with ra-

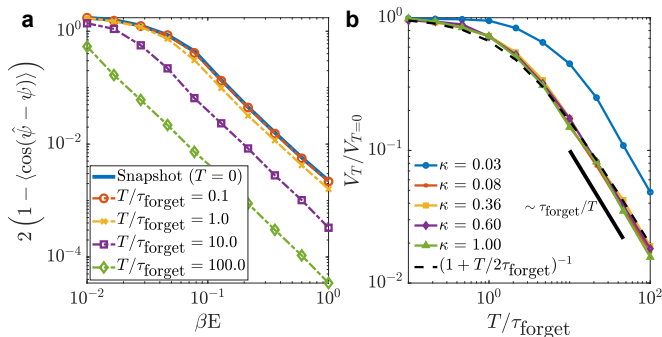


FIG. 5. To reduce error, cells must average over times long compared with τ_{forget} . **a:** Circular variance V_T as a function of $\kappa = \beta E$ for several averaging times T . **b:** V_T rescaled by its snapshot value $V_{T=0}$ behaves as $\sim \tau_{\text{forget}}/T$ at large averaging times. Lines are an average of 10 simulations of length $1000\tau_{\text{forget}}$, simulated with $\Delta t = 0.01\tau_{\text{forget}}$. Length of simulations were increased to $(0.1T/\tau_{\text{forget}}) \times 1000\tau_{\text{forget}}$ for $T/\tau_{\text{forget}} > 10$. This increase was capped at $5000\tau_{\text{forget}}$.

dius R , and potentially a little slower. This is reflected in Fig. 4. We start with the value γ fit for keratocytes in Fig. 3. Since we cannot separate β and N in our fit, we show a large range of values of N , and the corresponding values $\beta_0 = \gamma\sqrt{d/N} = \mu R_0/D$, where R_0 is the radius of the keratocyte. We then plot the directionality $\langle \cos(\hat{\psi} - \psi) \rangle$ as a function of R/R_0 . The results for different values of N collapse, as we expect. For these values of β , we are in the range $\kappa \ll 1$, and as in Fig. 2, the value of the directionality $\langle \cos(\hat{\psi} - \psi) \rangle$ found by summing sensor directions is smaller than expected by the bound. However, in both the sampled data and the bound, directionality depends weakly on radius.

Time-averaging to increase accuracy requires averaging times $\gtrsim R^2/D$. Cells or groups of cells sensing chemical concentrations or gradients may improve their accuracy by integrating multiple measurements of the signal over time [20, 33–36, 44, 45]. Broadly, we expect that making N_{meas} independent measurements of the gradient direction, reduces angular error by a factor of $\sqrt{N_{\text{meas}}}$, and that averaging over a time T would lead to $N_{\text{meas}} \sim T/\tau_{\text{corr}}$ independent measurements, where τ_{corr} is the correlation time of the measurement. If we rescale time in Eq. 1 to $\tilde{t} = t/\tau_{\text{forget}}$, where $\tau_{\text{forget}} \equiv R^2/D$ is the time for proteins to spread over the cell by diffusion in the absence of a field, we find

$$\frac{\partial}{\partial \tilde{t}} p(\theta, \tilde{t}) = \frac{\partial}{\partial \theta} [\kappa \sin \theta p(\theta, \tilde{t})] + \frac{\partial^2}{\partial \theta^2} p(\theta, \tilde{t}). \quad (8)$$

For a fixed value of κ , the only relevant timescale in the problem is then τ_{forget} . To study the effect of time-averaging, we perform a stochastic simulation of sensors moving in the field. The Langevin equation corresponding to Eq. 8 is

$$\frac{d}{d\tilde{t}} \theta_i(\tilde{t}) = -\kappa \sin \theta_i(\tilde{t}) + \xi(\tilde{t}), \quad (9)$$

where $\xi(\tilde{t})$ is a Gaussian white noise with $\langle \xi(\tilde{t})\xi(\tilde{t}') \rangle = 2\delta(\tilde{t} - \tilde{t}')$. We then simulate N independent sensors diffusing in the presence of the electric field by integrating Eq. 9 with the Euler-Maruyama method. We compute the time-averaged direction of the field as $\rho_T \equiv \frac{1}{T} \int_t^{t+T} dt' \rho(t')$, where $\rho(t) = \sum_i (\cos \theta_i(t), \sin \theta_i(t))$ is the sum of sensor positions as above. We then compute the circular variance V_T of the directions of the time-averaged estimator. Averaging does decrease error over a broad range of βE (Fig. 5a), though for $\beta E \lesssim 0.05$ this may be masked, since even with averaging, V_T is near its maximum of 2. As expected, for $T \ll \tau_{\text{forget}}$, the circular variance V_T limits back to the case of zero averaging time (Fig. 5b). For $T \gg \tau_{\text{forget}}$, the variance decreases as $\sim \tau_{\text{forget}}/T$, as our argument above would suggest. We can capture most of the effect of time-averaging with a form $V_T/V_{T=0} = \left(1 + \frac{T}{2\tau_{\text{forget}}}\right)^{-1}$ which we chose to match the expected asymptotic forms. However, at small enough κ , this collapse fails, again because V_T is reaching its maximum possible value of 2.

The time required to increase accuracy by averaging may be difficult for a cell to achieve. Allen et al. measured the time to forget for keratocytes to be roughly 15 minutes [5], consistent with a diffusion coefficient of $\sim 0.1 \mu\text{m}^2/\text{s}$. We see that in order to reduce error significantly, we must average over times significantly beyond τ_{forget} . By comparison, estimates of the integration time for Dictyostelium chemotaxis range from 2–20 s [19, 23, 25], and keratocytes can respond to new signals within 4–7 minutes [5].

Discussion. Our results imply that the optimal way for our circular or spherical cells to choose a direction of an electrical field is to simply sum the vectors pointing in the direction of their electromobile sensors. Surprisingly, this is exactly analogous to the estimator derived for chemotaxis of circular cells in [33, 34], where cells move toward the vector sum of their *bound* sensors. Optimal processing of galvanotactic information and chemotactic information could then be performed by signaling networks shared between galvanotactic and chemotactic responses. Supporting this idea, chemotactic and galvanotactic response in Dictyostelium share some common core elements, including TORC2 and PI3K [46].

A second key implication of our modeling is that the experimentally observed accuracy of galvanotaxis is physically plausible either with relatively few sensors (~ 100) that are as polarized as the observed level of tdTomato-GPI, or with a larger number of sensors that might be only weakly polarized even in strong (1000 V/m) electric fields. If the latter, a sensor need not have an immediately obvious redistribution. A natural experimental test of our result would be to simultaneously quantify, for a putative sensor, the abundance and polarization of the sensor and the cell's directionality as a function of field. A caveat to our analysis is that we have neglected downstream sources of noise – we assume that a cell's directionality $\langle \cos(\hat{\psi} - \psi) \rangle$ is controlled solely by the

stochasticity of sensor positions. In chemotaxis, we know that at stronger chemical gradients, when a cell has more information about the gradient orientation, other sources of noise may play a role [19], and similarly, we would expect the decrease in error shown in Fig. 2 to saturate at large fields if additional elements of cell motility, like noise in motility downstream of cell polarity [16], were included.

While earlier work on chemotaxis has largely been done in the shallow-gradient limit [33, 34] (though note [47]), our expressions for the Fisher information are valid for both weak and large electrical field strengths, and we note a transition between $I(\psi) \sim 1/(\beta E)^2$ at weak fields and $I(\psi) \sim 1/(\beta E)$ at high fields. This essentially corresponds to the point $\beta E \approx 1$ where the angular extent of the sensors becomes small enough that the von Mises distribution can be approximated as a Gaussian. However, transition in scaling may be difficult to detect in real cells: we have estimated $\beta E < 1$ for all the experiments studied, and at large fields we would expect downstream noise to be significant, as discussed above.

We have neglected sensor-sensor interactions in our analysis here. We expect these to only be relevant at very large fields and very large numbers of sensors. If

sensors were uniformly spread over the spherical cap region within $\pi/4$ of the field direction (this would be more concentrated than even $\kappa = 1$), the sensor density would be N/A with $A = 2\pi R^2(1 - \cos(\pi/4)) \approx 1.8R^2$. With $N = 10^4$ sensors and $R = 5 \mu\text{m}$, this is a typical distance between sensors of $\sqrt{A/N} \approx 70 \text{ nm}$, longer than typical screening lengths in biological systems. Hydrodynamic interactions in a membrane may in principle be long-range [48–50], and have been experimentally measured to be on the scale of a micron [51]. Including hydrodynamic interactions would not alter the steady-state probability distribution we found, but would lead the diffusion of the sensors to be correlated, changing the time required for the sensor configuration to decorrelate, likely only altering the prefactor on the scaling $\sim 1/T$ in Fig. 5b.

ACKNOWLEDGMENTS

We thank Wei Wang, Amit R. Singh, and Wouter-Jan Rappel for useful feedback and discussions. This material is based upon work supported by the National Science Foundation under Grant No. MCB 2119948 and PHY 1915491.

SUPPLEMENTARY INFORMATION

Appendix A: Periodic generalization of the Cramer-Rao bound

We show here a brief derivation of Eq. 7. This result can also be directly derived from a variant of the periodic Cramer-Rao bound found in [38], Chapter 5, but we show a derivation here because it is relatively straightforward but not well known in the physics literature. We start with a standard derivation of the ordinary Cramer-Rao bound, similar to, e.g., [39]. We use this here to show how the derivation of the periodic Cramer-Rao bound follows from similar logic.

a. Ordinary Cramer-Rao bound derivation

If we have a parameter ψ that we want to estimate from data \mathbf{x} , we can construct an estimator $\hat{\psi}(\mathbf{x})$. If the data is generated from a process with a probability density for the data given the parameter $p(\mathbf{x}|\psi)$, then requiring that the estimator is unbiased is requiring $\langle \hat{\psi} \rangle = \psi$ for all ψ i.e.

$$\int d\mathbf{x}(\hat{\psi}(\mathbf{x}) - \psi)p(\mathbf{x}|\psi) = 0. \quad (\text{A1})$$

Because this is true for all values of the parameter ψ , we can take a derivative:

$$\int d\mathbf{x}(\hat{\psi}(\mathbf{x}) - \psi)\frac{\partial}{\partial\psi}p(\mathbf{x}|\psi) - \int d\mathbf{x}p(\mathbf{x}|\psi) = 0. \quad (\text{A2})$$

The second term is just 1, since the probability density is normalized, so

$$1 = \int d\mathbf{x} (\hat{\psi}(\mathbf{x}) - \psi) \frac{\partial}{\partial \psi} p(\mathbf{x}|\psi), \quad (\text{A3})$$

$$1 = \int d\mathbf{x} (\hat{\psi}(\mathbf{x}) - \psi) p(\mathbf{x}|\psi) \frac{\partial}{\partial \psi} \ln p(\mathbf{x}|\psi), \quad (\text{A4})$$

$$1^2 = \left[\int d\mathbf{x} (\hat{\psi}(\mathbf{x}) - \psi) p(\mathbf{x}|\psi) \frac{\partial}{\partial \psi} \ln p(\mathbf{x}|\psi) \right]^2, \quad (\text{A5})$$

$$1 = \left[\int d\mathbf{x} \left\{ \sqrt{p(\mathbf{x}|\psi)} (\hat{\psi}(\mathbf{x}) - \psi) \right\} \left\{ \sqrt{p(\mathbf{x}|\psi)} \frac{\partial}{\partial \psi} \ln p(\mathbf{x}|\psi) \right\} \right]^2. \quad (\text{A6})$$

In the last line we have split p into $\sqrt{p}\sqrt{p}$. Then we can apply the Cauchy-Schwarz inequality, $(\int d\mathbf{x} f(\mathbf{x})g(\mathbf{x}))^2 \leq (\int d\mathbf{x} f(\mathbf{x})^2) (\int d\mathbf{x} g(\mathbf{x})^2)$, which gives

$$1 \leq \left[\int d\mathbf{x} p(\mathbf{x}|\psi) (\hat{\psi}(\mathbf{x}) - \psi)^2 \right] \left[\int d\mathbf{x} p(\mathbf{x}|\psi) \left(\frac{\partial}{\partial \psi} \ln p(\mathbf{x}|\psi) \right)^2 \right]. \quad (\text{A7})$$

Rearranging, this is

$$\langle (\hat{\psi} - \psi)^2 \rangle \geq \frac{1}{\left\langle \left(\frac{\partial}{\partial \psi} \ln p(\mathbf{x}|\psi) \right)^2 \right\rangle}. \quad (\text{A8})$$

The value $\left\langle \left(\frac{\partial}{\partial \psi} \ln p(\mathbf{x}|\psi) \right)^2 \right\rangle$ is $I(\psi)$, the Fisher information for ψ , and can be equivalently written as $\left\langle \left(\frac{\partial}{\partial \psi} \ln \mathcal{L} \right)^2 \right\rangle = -\left\langle \frac{\partial^2}{\partial \psi^2} \ln \mathcal{L} \right\rangle$ where $\mathcal{L}(\psi; \mathbf{x}) = p(\mathbf{x}|\psi)$ is the likelihood [39]. This establishes the ordinary Cramer-Rao bound (Eq. 6).

b. Generalization to periodic variables

The ordinary Cramer-Rao bound fails for periodic variables in part because the normal definition of an unbiased estimator, $\langle \hat{\psi} \rangle = \psi$, will not be reasonable when the variable to be estimated is only defined modulo 2π : $2\pi + \psi$ is just as good an estimate for ψ as ψ itself. We can define a generalized sense of ‘‘unbiased,’’ for a periodic variable, defining unbiased estimators $\hat{\psi}$ as having $\langle \sin(\hat{\psi} - \psi) \rangle = 0$ [38]. While we note that any estimator we can think of as having an unbiased direction will have $\langle \sin(\hat{\psi} - \psi) \rangle$, it would be possible to construct an estimator where $\hat{\psi} = \psi + \pi$ that also satisfy this constraint. Other periodic generalizations of the Cramer-Rao bound exist, with different definitions of periodic unbiasedness, e.g. [52]. However, these generally require knowledge of the distribution of the estimator $\hat{\psi}$ in order to construct the bound, making them less useful in our context. The bound we will derive here, while correct, may be able to be improved.

Beginning with this definition of an unbiased estimator,

$$\int d\mathbf{x} \sin(\hat{\psi}(\mathbf{x}) - \psi) p(\mathbf{x}|\psi) = 0. \quad (\text{A9})$$

We can take a derivative with respect to the parameter ψ :

$$\int d\mathbf{x} \sin(\hat{\psi}(\mathbf{x}) - \psi) \frac{\partial}{\partial \psi} p(\mathbf{x}|\psi) - \int d\mathbf{x} p(\mathbf{x}|\psi) \cos(\hat{\psi}(\mathbf{x}) - \psi) = 0. \quad (\text{A10})$$

The second term is just $-\langle \cos(\hat{\psi} - \psi) \rangle$. We can then follow a similar approach to the previous section,

$$\int d\mathbf{x} \sin(\hat{\psi}(\mathbf{x}) - \psi) p(\mathbf{x}|\psi) \frac{\partial}{\partial \psi} \ln p(\mathbf{x}|\psi) = \langle \cos(\hat{\psi} - \psi) \rangle, \quad (\text{A11})$$

$$\left[\int d\mathbf{x} \sqrt{p(\mathbf{x}|\psi)} \sin(\hat{\psi}(\mathbf{x}) - \psi) \sqrt{p(\mathbf{x}|\psi)} \frac{\partial}{\partial \psi} \ln p(\mathbf{x}|\psi) \right]^2 = \langle \cos(\hat{\psi} - \psi) \rangle^2. \quad (\text{A12})$$

Applying Cauchy-Schwarz,

$$\langle \cos(\hat{\psi} - \psi) \rangle^2 \leq \left[\int d\mathbf{x} p(\mathbf{x}|\psi) \sin^2(\hat{\psi}(\mathbf{x}) - \psi) \right] \left[\int d\mathbf{x} p(\mathbf{x}|\psi) \left(\frac{\partial}{\partial \psi} \ln p(\mathbf{x}|\psi) \right)^2 \right], \quad (\text{A13})$$

$$\langle \cos(\hat{\psi} - \psi) \rangle^2 \leq \langle \sin^2(\hat{\psi} - \psi) \rangle I(\psi). \quad (\text{A14})$$

This bound is the analogous bound to the Cramer-Rao bound, but unfortunately this bound depends not only on the Fisher information $I(\psi)$ but also $\langle \sin^2(\hat{\psi} - \psi) \rangle$ – making it difficult to apply when we do not know the distribution of $\hat{\psi}$. We can get a more easily applied result – at the cost of weakening the bound slightly. We start by rewriting $\langle \sin^2(\hat{\psi} - \psi) \rangle = 1 - \langle \cos^2(\hat{\psi} - \psi) \rangle$. Then

$$\cos(\hat{\psi} - \psi)^2 \leq \left(1 - \langle \cos^2(\hat{\psi} - \psi) \rangle \right) I(\psi). \quad (\text{A15})$$

Because $\langle \cos^2(\hat{\psi} - \psi) \rangle \geq \langle \cos(\hat{\psi} - \psi) \rangle^2$ (by the positivity of the variance, or the Cauchy-Schwarz inequality again),

$$\langle \cos(\hat{\psi} - \psi) \rangle^2 \leq \left(1 - \langle \cos(\hat{\psi} - \psi) \rangle^2 \right) I(\psi), \quad (\text{A16})$$

$$[1 + I(\psi)] \langle \cos(\hat{\psi} - \psi) \rangle^2 \leq I(\psi), \quad (\text{A17})$$

$$\langle \cos(\hat{\psi} - \psi) \rangle \leq \sqrt{\frac{I(\psi)}{1 + I(\psi)}}. \quad (\text{A18})$$

This is Eq. 7 in the main text. This reduces to the ordinary Cramer-Rao bound in the limit of large $I(\psi)$, in which case we expect the distribution of $\hat{\psi}$ becomes closely localized to ψ , so $\langle \cos(\hat{\psi} - \psi) \rangle \approx 1 - \frac{1}{2} \langle (\hat{\psi} - \psi)^2 \rangle$. Simultaneously, $\sqrt{I/(1+I)} = \sqrt{1/(I^{-1}+1)} \approx 1 - \frac{1}{2I}$, so the bound Eq. 7 becomes Eq. 6.

Appendix B: Fisher information and estimation of field magnitude

In the main paper, we have introduced the Fisher information for the field direction only. However, it is straightforward to extend the results to describe simultaneous estimation of the field direction and strength. Simultaneously estimating the field strength does not change the accuracy of the directional estimate – as we might guess, because the estimator for the field direction – the sum of sensor directions – doesn't depend on field strength.

The probability density of a single sensor is $p(\theta) = Z^{-1} e^{\kappa \cos(\theta - \psi)}$. For $p(\theta)$ to integrate to one, $Z = 2\pi I_0(\kappa)$. We note $\kappa = \beta E$. Then the log-likelihood is (from Eq. 3),

$$\ln \mathcal{L}(\psi, E; \boldsymbol{\theta}) = -N \ln [2\pi I_0(\kappa)] + \kappa \sum_{i=1}^N \cos(\theta_i - \psi). \quad (\text{B1})$$

Then we can work out the Fisher information matrix $\mathcal{I} = -\langle \frac{\partial^2 \ln \mathcal{L}}{\partial \alpha \partial \beta} \rangle$ where α, β are dummy variables indicating field magnitude E or angle ψ . To do this, we compute:

$$\left\langle \frac{\partial^2}{\partial \psi^2} \ln \mathcal{L}(\psi, E; \boldsymbol{\theta}) \right\rangle = -\kappa \sum_{i=1}^N \langle \cos(\theta_i - \psi) \rangle, \quad (\text{B2})$$

$$\left\langle \frac{\partial^2}{\partial \psi \partial E} \ln \mathcal{L}(\psi, E; \boldsymbol{\theta}) \right\rangle = \beta \sum_{i=1}^N \langle \sin(\theta_i - \psi) \rangle, \quad (\text{B3})$$

$$\left\langle \frac{\partial^2}{\partial E^2} \ln \mathcal{L}(\psi, E; \boldsymbol{\theta}) \right\rangle = -N \frac{\beta^2}{2} \left[1 + \frac{I_2(\kappa)}{I_0(\kappa)} - 2 \left(\frac{I_1(\kappa)}{I_0(\kappa)} \right)^2 \right]. \quad (\text{B4})$$

The expectation of the cosine is $\langle \cos(\theta_i - \psi) \rangle = I_1(\kappa)/I_0(\kappa)$ and $\langle \sin(\theta_i - \psi) \rangle = 0$ by symmetry.

This gives us the final Fisher information matrix \mathcal{I} ,

$$\mathcal{I} = N \begin{pmatrix} \kappa \frac{I_1(\kappa)}{I_0(\kappa)} & 0 \\ 0 & \frac{\beta^2}{2} \left[1 + \frac{I_2(\kappa)}{I_0(\kappa)} - 2 \left(\frac{I_1(\kappa)}{I_0(\kappa)} \right)^2 \right] \end{pmatrix}. \quad (\text{B5})$$

These results are known as the Fisher information associated with multiple samples of a von Mises distribution [38].

Appendix C: Calculation of Fisher information for a spherical cell

The concentration of sensors on a spherical cell with an electric field in the z direction is worked out in [37] as $c \sim e^{\beta E \cos \theta}$. We can generalize this to a field in an arbitrary direction as $p(\theta, \phi) \sim \exp(\beta \mathbf{E} \cdot \hat{\mathbf{u}})$, where $\hat{\mathbf{u}} = (\cos \phi \sin \theta, \sin \phi \sin \theta, \cos \theta)$ is the unit vector on the sphere – this is the von Mises-Fisher distribution [38]. To model a cell on a substrate, where velocities can only be measured in the plane of the substrate, we will assume explicitly that the field is in the xy plane. We can then, considering the field angle relative to the x axis as ψ , write the probability distribution of a single sensor as $p(\phi, \theta) = Z^{-1} \exp[\kappa \cos(\phi - \psi) \sin \theta]$. For $\int d\theta \sin \theta d\phi p(\phi, \theta) = 1$, we have $Z = (4\pi \sinh \kappa)/\kappa$. Then, similar to Eq. 3, the log-likelihood takes the form

$$\ln \mathcal{L}(\psi, E; \boldsymbol{\theta}) = N \ln \left[\frac{\kappa}{4\pi \sinh \kappa} \right] + \kappa \sum_{i=1}^N \cos(\phi_i - \psi) \sin \theta_i. \quad (\text{C1})$$

We note that the second term on the right can be rewritten, so that the log-likelihood is

$$\ln \mathcal{L}(\psi, E; \boldsymbol{\theta}) = N \ln \left[\frac{\kappa}{4\pi \sinh \kappa} \right] + \beta \sum_{i=1}^N \mathbf{E} \cdot \hat{\mathbf{u}}_i^{xy}, \quad (\text{C2})$$

$$= N \ln \left[\frac{\kappa}{4\pi \sinh \kappa} \right] + \beta \mathbf{E} \cdot \boldsymbol{\rho}^{xy}, \quad (\text{C3})$$

where $\hat{\mathbf{u}}_i^{xy} = (\cos \phi_i \sin \theta_i, \sin \phi_i \sin \theta_i, 0)$ and $\boldsymbol{\rho}^{xy} = \sum_i \hat{\mathbf{u}}_i^{xy}$ is the sum of the sensor locations – projected into the xy plane. The orientation of the field $\mathbf{E} = E(\cos \psi, \sin \psi, 0)$ that maximizes the likelihood is the one that puts \mathbf{E} in line with $\boldsymbol{\rho}^{xy}$, exactly as in the 2D circle case; (we can also see this by explicitly differentiating the log-likelihood; see Appendix D.)

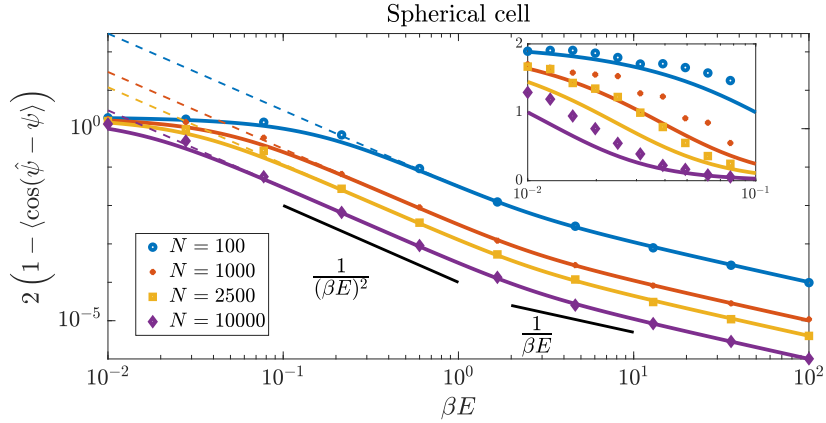


FIG. 6. Accuracy of galvanotactic estimation as a function of electric field and number of sensors for a spherical cell. Solid lines are the simple periodic bound (Eq. 7), dashed lines are the normal Cramer-Rao bound (Eq. 6), symbols are computed from stochastic simulation. Inset shows zoomed in region in linear spacing, showing MLE variance is systematically above Eq. 7.

Now we can compute the Fisher information like we did for the circle by first calculating the second derivatives:

$$\left\langle \frac{\partial^2}{\partial \psi^2} \ln \mathcal{L}(\psi, E; \boldsymbol{\theta}) \right\rangle = -\kappa \sum_{i=1}^N \langle \cos(\phi_i - \psi) \sin \theta_i \rangle, \quad (\text{C4})$$

$$\left\langle \frac{\partial^2}{\partial \psi \partial E} \ln \mathcal{L}(\psi, E; \boldsymbol{\theta}) \right\rangle = \beta \sum_{i=1}^N \langle \sin(\phi_i - \psi) \sin \theta_i \rangle, \quad (\text{C5})$$

$$\left\langle \frac{\partial^2}{\partial E^2} \ln \mathcal{L}(\psi, E; \boldsymbol{\theta}) \right\rangle = -N \beta^2 \frac{\sinh^2 \kappa - \kappa^2}{\kappa^2 \sinh^2 \kappa}. \quad (\text{C6})$$

The expectation values $\langle \cos(\phi_i - \psi) \sin \theta_i \rangle = \kappa^{-1}(\kappa \coth \kappa - 1)$ and $\langle \sin(\phi_i - \psi) \sin \theta_i \rangle = 0$ by symmetry. By taking

the negatives of the calculated derivatives, this gives us the final Fisher information matrix \mathcal{I} ,

$$\mathcal{I} = N \begin{pmatrix} \kappa \coth \kappa - 1 & 0 \\ 0 & \beta^2 \frac{\sinh^2 \kappa - \kappa^2}{\kappa^2 \sinh^2 \kappa} \end{pmatrix}. \quad (\text{C7})$$

The upper-left component of the matrix corresponds to $I(\psi)$, which was given as Eq. 5 in the main text.

We show the spherical-cell analog to Fig. 2 in Fig. 6. Here, the stochastic simulation is done by generating random sensors according to $p(\phi, \theta) \sim Z^{-1} \exp[\kappa \cos(\phi - \psi) \sin \theta]$ by rejection sampling (we note that to sample from this distribution on the sphere, we are sampling from $p(\phi, \theta) \sin \theta d\theta d\phi$). For each parameter, we generate 1000 sensor configurations. For each configuration, we compute the estimator $\hat{\psi}$ by summing sensor positions to find ρ^{xy} , and then use this to compute V .

The results of Fig. 4 can also be generalized to the spherical cell assumption, and do not depend strongly on this change (Fig. 7). This is, of course, what we would expect, because the Fisher information $I(\psi)$ differs only by a

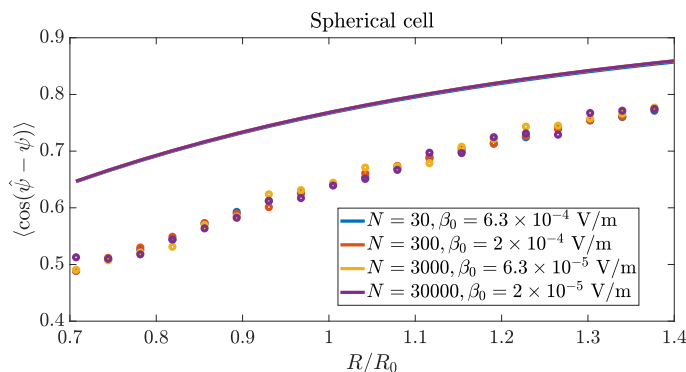


FIG. 7. Equivalent of Fig. 4 assuming a spherical cell. Lines are the bound (Eq. 7 with Eq. 5), symbols are stochastic simulation, as in Fig. 2. $\gamma^2 = N\beta^2/d$ is fit to the data of [43], $\gamma = 0.002$ m/V, and the E field used is 600 V/m. $d = 3$.

constant factor between $d = 2$ and $d = 3$, and this factor has been absorbed into γ . We can only extract γ from the data in Fig. 3, but we also only need γ to reliably predict the radius-dependence.

Appendix D: Computing maximum likelihood estimators for field direction and strength

We discuss in the main text that the optimal way for round cells to choose a direction of an electrical field is to sum the vectors pointing in the direction of their electromobile sensors. We argued in the main text that this maximizes the likelihood. Here we show this a little more explicitly, as well as showing how estimators for the electric field magnitude can be derived. The log-likelihood functions for a circular and spherical cell are given by Eqs. B1 and C1, respectively. To find the maximum likelihood estimator, we find the value $\hat{\psi}$ that maximizes these log-likelihoods by differentiating each equation with ψ and setting this equal to zero,

$$\text{Circle : } \left. \frac{\partial}{\partial \psi} \ln \mathcal{L}(\psi, E; \boldsymbol{\theta}) \right|_{\psi=\hat{\psi}} = \kappa \sum_{i=1}^N \sin(\theta_i - \hat{\psi}) = 0, \quad (\text{D1})$$

$$\text{Sphere : } \left. \frac{\partial}{\partial \psi} \ln \mathcal{L}(\psi, E; \boldsymbol{\theta}) \right|_{\psi=\hat{\psi}} = \kappa \sum_{i=1}^N \sin(\phi_i - \hat{\psi}) \sin \theta_i = 0. \quad (\text{D2})$$

For the circle, we can solve for $\hat{\psi}$ by using the trigonometric identity $\sum \sin(\theta_i - \hat{\psi}) = \sum (\sin \theta_i \cos \hat{\psi} - \cos \theta_i \sin \hat{\psi}) = 0$. Separating the two terms allows us to factor out $\hat{\psi}$ from the summation: $\cos \hat{\psi} \sum \sin \theta_i = \sin \hat{\psi} \sum \cos \theta_i$. From this juncture, we can then solve for the estimator, $\hat{\psi}$, of the field direction. An analogous calculation can be done for the

sphere. These results are:

$$\text{Circle : } \tan \hat{\psi} = \frac{\sum_{i=1}^N \sin \theta_i}{\sum_{i=1}^N \cos \theta_i}, \quad (\text{D3})$$

$$\text{Sphere : } \tan \hat{\psi} = \frac{\sum_{i=1}^N \sin \phi_i \sin \theta_i}{\sum_{i=1}^N \cos \phi_i \sin \theta_i}. \quad (\text{D4})$$

We see that the optimal angle is obtained from the components of the summed vector of the sensor locations, $\boldsymbol{\rho}$.

In addition, we can find the maximum likelihood estimator for the field strength E . Differentiating the log-likelihood functions for the circle and sphere for the field strength, E , yields:

$$\text{Circle : } \left. \frac{\partial}{\partial E} \ln \mathcal{L}(\psi, E; \boldsymbol{\theta}) \right|_{E=\hat{E}} = \beta \sum_{i=1}^N \cos(\theta_i - \psi) - \beta N \frac{I_1(\hat{\kappa})}{I_0(\hat{\kappa})} = 0, \quad (\text{D5})$$

$$\text{Sphere : } \left. \frac{\partial}{\partial E} \ln \mathcal{L}(\psi, E; \boldsymbol{\theta}) \right|_{E=\hat{E}} = \beta \sum_{i=1}^N \cos(\phi_i - \psi) \sin \theta_i + \frac{N}{\hat{E}} - \frac{N\beta}{\tanh \hat{\kappa}} = 0. \quad (\text{D6})$$

where $\hat{\kappa} = \beta \hat{E}$. We can then reorganize these equations to provide formulas for the maximum likelihood estimators.

$$\text{Circle : } \frac{I_1(\hat{\kappa})}{I_0(\hat{\kappa})} = \frac{1}{N} \sum_{i=1}^N \cos(\theta_i - \psi), \quad (\text{D7})$$

$$\text{Sphere : } \frac{1}{\hat{\kappa}} (\hat{\kappa} \coth \hat{\kappa} - 1) = \frac{1}{N} \sum_{i=1}^N \cos(\phi_i - \psi) \sin \theta_i. \quad (\text{D8})$$

We cannot analytically solve for the electric field here, but this provides a straightforward numerical way to find the maximum likelihood estimator \hat{E} .

-
- [1] S. SenGupta, C. A. Parent, and J. E. Bear, The principles of directed cell migration, *Nature Reviews Molecular Cell Biology*, 1 (2021).
 - [2] A. S. Kennard and J. A. Theriot, Osmolarity-independent electrical cues guide rapid response to injury in zebrafish epidermis, *eLife* **9**, e62386 (2020).
 - [3] Y. Sun, B. Reid, F. Ferreira, G. Luxardi, L. Ma, K. L. Lokken, K. Zhu, G. Xu, Y. Sun, V. Ryzhuk, *et al.*, Infection-generated electric field in gut epithelium drives bidirectional migration of macrophages, *PLoS Biology* **17**, e3000044 (2019).
 - [4] M. Zhao, Electrical fields in wound healing—an overriding signal that directs cell migration, in *Seminars in Cell & Developmental Biology*, Vol. 20 (Elsevier, 2009) pp. 674–682.
 - [5] G. M. Allen, A. Mogilner, and J. A. Theriot, Electrophoresis of cellular membrane components creates the directional cue guiding keratocyte galvanotaxis, *Current Biology* **23**, 560 (2013).
 - [6] B. M. Kobylkevich, A. Sarkar, B. R. Carlberg, L. Huang, S. Ranjit, D. M. Graham, and M. A. Messerli, Reversing the direction of galvanotaxis with controlled increases in boundary layer viscosity, *Physical Biology* **15**, 036005 (2018).
 - [7] A. Sarkar, B. M. Kobylkevich, D. M. Graham, and M. A. Messerli, Electromigration of cell surface macromolecules in dc electric fields during cell polarization and galvanotaxis, *Journal of Theoretical Biology* **478**, 58 (2019).
 - [8] N. Ogawa, H. Oku, K. Hashimoto, and M. Ishikawa, A physical model for galvanotaxis of paramecium cell, *Journal of Theoretical Biology* **242**, 314 (2006).
 - [9] T. J. Zajdel, G. Shim, L. Wang, A. Rossello-Martinez, and D. J. Cohen, SCHEEPDOG: programming electric cues to dynamically herd large-scale cell migration, *Cell Systems* **10**, 506 (2020).
 - [10] G. Shim, D. Devenport, and D. J. Cohen, Overriding native cell coordination enhances external programming of collective cell migration, *Proceedings of the National Academy of Sciences* **118** (2021).
 - [11] M. L. Lalli and A. R. Asthagiri, Collective migration exhibits greater sensitivity but slower dynamics of alignment to applied electric fields, *Cellular and Molecular Bioengineering* **8**, 247 (2015).
 - [12] J. E. Dawson, T. Sellmann, K. Porath, R. Bader, U. van Rienen, R. Appali, and R. Köhling, Computational model for migration of human osteoblasts in direct current electric field, *bioRxiv*, 2020 (2021).
 - [13] Y. Sun, H. Yue, C. Copos, K. Zhu, Y. Zhang, X. Gao, Y. Sun, B. Reid, F. Lin, M. Zhao, *et al.*, PI3K inhibition reverses migratory direction of single cells but not cell groups in electric field, *bioRxiv* (2020).
 - [14] Y. Zhang, G. Xu, J. Wu, R. M. Lee, Z. Zhu, Y. Sun, K. Zhu, W. Losert, S. Liao, G. Zhang, *et al.*, Propagation dynamics of electrotactic motility in large epithelial cell sheets, *bioRxiv* (2022).

- [15] T. P. Prescott, K. Zhu, M. Zhao, and R. E. Baker, Quantifying the impact of electric fields on single-cell motility, *Biophysical Journal* **120**, 3363–3373 (2021).
- [16] I. Nwogbaga and B. A. Camley, Self-propelled deformable particle model for keratocyte galvanotaxis, arXiv preprint arXiv:2204.01589 (2022).
- [17] H. Gruler and R. Nuccitelli, Neural crest cell galvanotaxis: new data and a novel approach to the analysis of both galvanotaxis and chemotaxis, *Cell motility and the cytoskeleton* **19**, 121 (1991).
- [18] M. Schienbein and H. Gruler, Langevin equation, Fokker-Planck equation and cell migration, *Bulletin of Mathematical Biology* **55**, 585 (1993).
- [19] D. Fuller, W. Chen, M. Adler, A. Groisman, H. Levine, W.-J. Rappel, and W. F. Loomis, External and internal constraints on eukaryotic chemotaxis, *Proceedings of the National Academy of Sciences* **107**, 9656 (2010).
- [20] H. C. Berg and E. M. Purcell, Physics of chemoreception, *Biophysical Journal* **20**, 193 (1977).
- [21] H. Mattingly, K. Kamino, B. Machta, and T. Emonet, *Escherichia coli* chemotaxis is information limited, *Nature Physics* **17**, 1426 (2021).
- [22] B. W. Andrews and P. A. Iglesias, An information-theoretic characterization of the optimal gradient sensing response of cells, *PLoS Computational Biology* **3**, e153 (2007).
- [23] I. Segota, S. Mong, E. Neidich, A. Rachakonda, C. J. Lussenhop, and C. Franck, High fidelity information processing in folic acid chemotaxis of *Dictyostelium amoebae*, *Journal of The Royal Society Interface* **10**, 20130606 (2013).
- [24] L. Song, S. M. Nadkarni, H. U. Bödeker, C. Beta, A. Bae, C. Franck, W.-J. Rappel, W. F. Loomis, and E. Bodenschatz, *Dictyostelium discoideum* chemotaxis: threshold for directed motion, *European Journal of Cell Biology* **85**, 981 (2006).
- [25] P. J. Van Haastert and M. Postma, Biased random walk by stochastic fluctuations of chemoattractant-receptor interactions at the lower limit of detection, *Biophysical Journal* **93**, 1787 (2007).
- [26] E. P. Ipiña and B. A. Camley, Collective gradient sensing with limited positional information, *Physical Review E* **105**, 044410 (2022).
- [27] S. Fancher and A. Mugler, Fundamental limits to collective concentration sensing in cell populations, *Physical review letters* **118**, 078101 (2017).
- [28] S. Fancher, M. Vennettilli, N. Hilgert, and A. Mugler, Precision of flow sensing by self-communicating cells, *Physical review letters* **124**, 168101 (2020).
- [29] M. Vennettilli, S. Saha, U. Roy, and A. Mugler, Precision of protein thermometry, *Physical Review Letters* **127**, 098102 (2021).
- [30] W. Bialek and S. Setayeshgar, Physical limits to biochemical signaling, *Proceedings of the National Academy of Sciences* **102**, 10040 (2005).
- [31] T. Mora and I. Nemenman, Physical limit to concentration sensing in a changing environment, *Physical review letters* **123**, 198101 (2019).
- [32] R. G. Endres and N. S. Wingreen, Maximum likelihood and the single receptor, *Physical Review Letters* **103**, 158101 (2009).
- [33] B. Hu, W. Chen, W.-J. Rappel, and H. Levine, Physical limits on cellular sensing of spatial gradients, *Physical Review Letters* **105**, 048104 (2010).
- [34] B. Hu, W. Chen, W.-J. Rappel, and H. Levine, How geometry and internal bias affect the accuracy of eukaryotic gradient sensing, *Physical Review E* **83**, 021917 (2011).
- [35] A. Hopkins and B. A. Camley, Chemotaxis in uncertain environments: Hedging bets with multiple receptor types, *Physical Review Research* **2**, 043146 (2020).
- [36] B. A. Camley and W.-J. Rappel, Cell-to-cell variation sets a tissue-rheology-dependent bound on collective gradient sensing, *Proceedings of the National Academy of Sciences* **114**, E10074 (2017).
- [37] S. McLaughlin and M. Poo, The role of electro-osmosis in the electric-field-induced movement of charged macromolecules on the surfaces of cells, *Biophysical Journal* **34**, 85 (1981).
- [38] K. V. Mardia and P. E. Jupp, *Directional statistics*, Vol. 2 (Wiley Online Library, 2000).
- [39] S. M. Kay, *Fundamentals of statistical signal processing: estimation theory* (Prentice-Hall, Inc., 1993).
- [40] K. S. Fang, E. Ionides, G. Oster, R. Nuccitelli, and R. R. Isseroff, Epidermal growth factor receptor relocalization and kinase activity are necessary for directional migration of keratinocytes in dc electric fields, *Journal of Cell Science* **112**, 1967 (1999).
- [41] J. L. Macdonald and L. J. Pike, Heterogeneity in EGF-binding affinities arises from negative cooperativity in an aggregating system, *Proceedings of the National Academy of Sciences* **105**, 112 (2008).
- [42] B.-j. Lin, S.-h. Tsao, A. Chen, S.-K. Hu, L. Chao, and P.-h. G. Chao, Lipid rafts sense and direct electric field-induced migration, *Proceedings of the National Academy of Sciences* **114**, 8568 (2017).
- [43] Y. Sun, H. Do, J. Gao, R. Zhao, M. Zhao, and A. Mogilner, Keratocyte fragments and cells utilize competing pathways to move in opposite directions in an electric field, *Current Biology* **23**, 569 (2013).
- [44] P. R. ten Wolde, N. B. Becker, T. E. Ouldridge, and A. Mugler, Fundamental limits to cellular sensing, *Journal of Statistical Physics* **162**, 1395 (2016).
- [45] B. A. Camley, Collective gradient sensing and chemotaxis: modeling and recent developments, *Journal of Physics: Condensed Matter* **30**, 223001 (2018).
- [46] R. Gao, S. Zhao, X. Jiang, Y. Sun, S. Zhao, J. Gao, J. Borleis, S. Willard, M. Tang, H. Cai, *et al.*, A large-scale screen reveals genes that mediate electrotaxis in *Dictyostelium discoideum*, *Science Signaling* **8**, ra50 (2015).
- [47] A. Hopkins and B. A. Camley, Leader cells in collective chemotaxis: Optimality and trade-offs, *Physical Review E* **100**, 032417 (2019).

- [48] E. Noruzifar, B. A. Camley, and F. L. Brown, Calculating hydrodynamic interactions for membrane-embedded objects, *The Journal of Chemical Physics* **141**, 124711 (2014).
- [49] N. Oppenheimer and H. Diamant, Correlated diffusion of membrane proteins and their effect on membrane viscosity, *Biophysical Journal* **96**, 3041 (2009).
- [50] N. Oppenheimer and H. Diamant, In-plane dynamics of membranes with immobile inclusions, *Physical Review Letters* **107**, 258102 (2011).
- [51] M. Chein, E. Perlson, and Y. Roichman, Flow arrest in the plasma membrane, *Biophysical Journal* **117**, 810 (2019).
- [52] T. Routtenberg and J. Tabrikian, Periodic CRB for non-Bayesian parameter estimation, in *2011 IEEE International Conference on Acoustics, Speech and Signal Processing (ICASSP)* (IEEE, 2011) pp. 2448–2451.